# Effect of Subsonic Mach Number on Cavity Acoustics

S. Argha*, O. N. Ramesh* and N. Balakrishnan*
Corresponding author: arghasaha@iisc.ac.in
* Aerospace Engineering Department, IISc Bangalore, India.

*Keywords:* Cavity Noise, Mach Effect, Aeroacoustics, Detached Eddy Simulation.

## 1. Introduction

Combat aircraft typically carry weapons within concealed bays; however, during weapon release, unsteady acoustic–structure interactions dominate over other aerodynamic phenomena, and this effect becomes increasingly severe with increasing cruise speed. Despite significant advances, starting from the celebrated work of Rossiter [1] to the more recent studies by Sun et al. [2] and Mathias and Medeiros [3], in understanding the influence of Mach number on cavity acoustics, several key issues remain unresolved, particularly the statistical origin of the observed increase in acoustic levels and the manner in which increasing compressibility alters the temporal organization, intermittency, and modal dynamics of cavity oscillations. A transitional-open type of cavity with length to depth (L/D) ratio of 6.25 and width to depth (W/D) ratio of 2 has been chosen to gain a deeper understanding of the acoustic noise characteristic. To achieve a trade off between the computational cost and accurate representation, Detached Eddy Simulations are performed. Initially, the simulation methodology was established in HiFUN [4] and validated against an experimental study by Rokita et al [5]. The oncoming velocity profile at a location upstream of the cavity front wall and the mean Cp profile at the cavity mid-plane are first matched with the experiments before a comparison is carried forward on the fluctuation data. From this standpoint, a further analysis is performed to investigate the dependence of the cavity acoustic field on Mach number.

## 2. Methodology

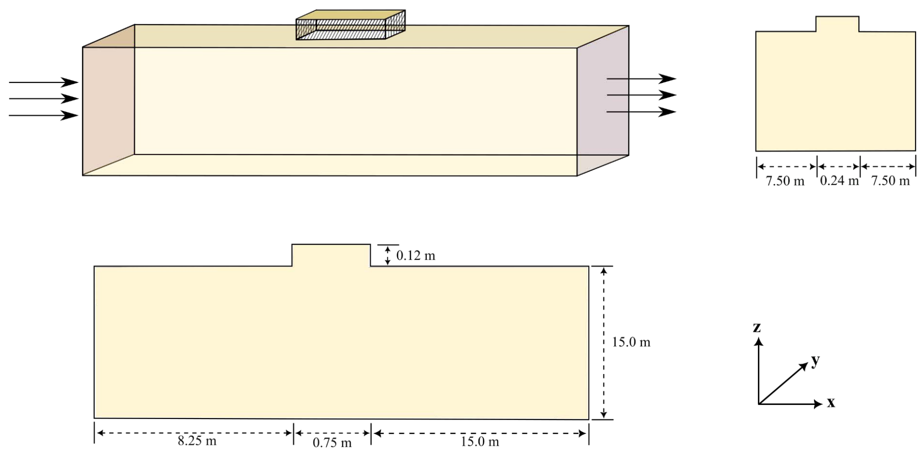


Figure 1: Schematic of the flow domain for the validation case (not to scale)

A three-dimensional computational domain is adopted, as shown in Fig. 1. The cavity geometry and flow conditions are identical to those in the experiment of Rokita et al. [5], and the upstream wall length is adjusted to match the boundary-layer characteristics immediately before the cavity leading edge. The reference experiments were conducted in a tunnel with porous non-reflecting walls. Accordingly, to mimic the experimental flow environment, the cavity together with the tunnel top wall is immersed in

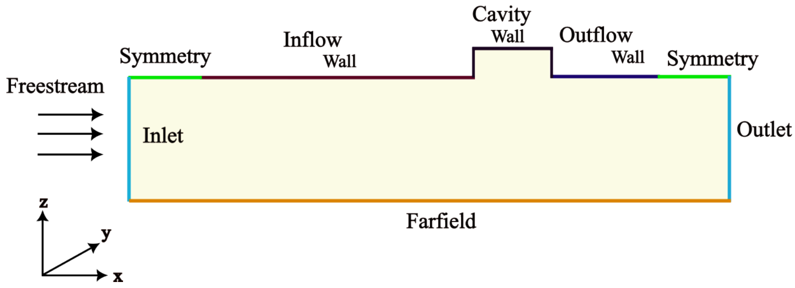


Figure 2: 2D representation of the 3D domain with boundary conditions

a freestream corresponding to a Mach number of 0.4. Towards the objective of capturing the effect at various Mach numbers, the Reynolds number based on the upstream momentum thickness at the desired location and the cavity geometry, which is the same as that used by Rokita et al. [5] in their experiment, are kept constant, while the Mach number is systematically varied from 0.4 to 0.8.

The cavity walls are modeled using no-slip boundary conditions, while the tunnel top wall is represented using a combination of symmetry (inviscid wall) and no-slip boundary conditions, as illustrated in Fig. 2. Inflow and outflow are prescribed using the pressure inlet and pressure outlet boundary conditions available in the HiFUN solver, where the inlet maintains the total dynamic head and the outlet enforces the static pressure. Non-reflecting far-field boundary conditions are applied on the remaining three sides of the computational domain. The Symmetry condition is used downstream to extend the flow domain. This condition enforces the inviscid flow characteristics in the specified region of the tunnel. The computational domain consists of approximately 24 million mesh volumes, with 90% of the volumes concentrated within the cavity and its shear layer region. To accurately capture the flow physics in these critical areas, mesh embedding strategy available in HiFUN solver is employed twice. This refinement is applied over the base mesh, which was initially generated using ICEM CFD. The final refined mesh can easily capture the minimum wavelength corresponding to the maximum target frequency. Additionally, for efficient utilization of the DES strategy, the grid spacing in the cavity was chosen such that $\Delta x : \Delta y : \Delta z = 3 : 2 : 1$.

Unsteady DES simulations are initialized using converged RANS solutions. A time step of $10^{-5}$ sec was chosen as it was found to be adequate in capturing the required pressure fluctuations. Prior to this selection, the maximum expected frequency was estimated, and the corresponding Nyquist criterion was conservatively satisfied to ensure adequate temporal resolution. For the unsteady DES simulations, convergence in the inner dual time loop was declared for a residual drop of $10^{-4}$ which was consistently achieved within 30 steps in the dual time loop for all computations. Both spatial and temporal discretizations are second-order accurate. For the time integration, a dual time-stepping based implicit BDF2 procedure is utilized. Roe scheme and Green-Gauss procedure are employed for the inviscid and viscous flux calculations, respectively. $k$–$\omega$ SST turbulence model is used as it was found to be the best suited for this class of unsteady simulations.

## 3. Results and Discussion

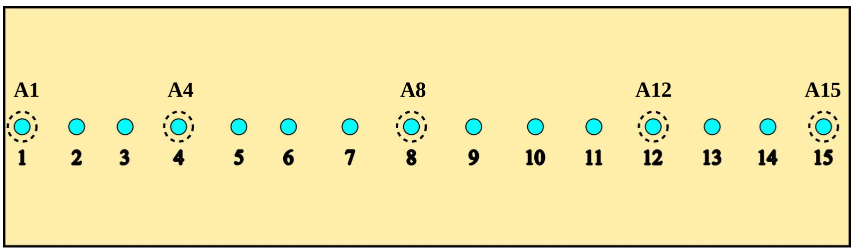


Figure 3: Probe locations at the cavity top wall

The results at Mach 0.4 are first compared with the available experimental data to validate the simulation procedure. Three primary quantities are examined: the oncoming velocity profile, the mean Cp distribution at the cavity mid-plane, and the sound pressure level (SPL) spectra at five locations on the cavity top wall represented by A1, A4, A8, A12 and A15 as in Fig. 3. In all cases, the numerical results show close agreement with the experimental measurements. Detailed validation results and error characterization have already been documented in the study by Saha et al. [6].

### 3.1 Mach Number Effect - SPL and other Mean profile comparison

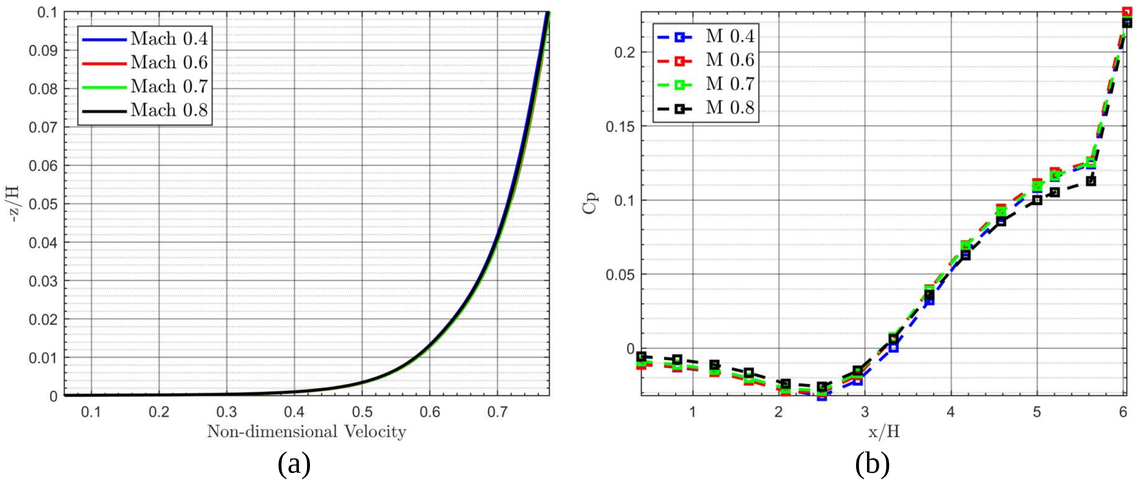


Figure 4: Inflow velocity profile (a) and mean Cp distribution at the cavity top mid plane (b) for all Mach numbers

In Fig. 4(a) non-dimensional incoming velocity profiles have been plotted for an upstream location at the cavity leading edge ($x/H = -0.2$). Across the evaluated Mach sweep (0.4 to 0.8), the normalized velocity profiles collapse almost perfectly. This confirms that, despite increasing compressibility, the incoming boundary layer retains a consistent mean shape.

Fig. 4(b) illustrates the corresponding mean surface pressure coefficient ($C_p$) distribution along the cavity mid-plane. All Mach numbers show the same overall trend. A mild pressure drop just after the leading edge marks where the flow separates and the free shear layer begins. The pressure then recovers and rises sharply at the trailing edge. This sharp rise marks the exact point where the shear layer violently strikes the back wall.

Fig. 5 shows the Sound Pressure Level (SPL) distribution across five locations (shown in Fig. 3) along the cavity top. At every Mach number, distinct tonal peaks — corresponding to classical Rossiter modes, appear across the entire cavity length. Importantly, these peaks are clearly visible right after the leading edge (i.e. at A1 location). This indicates that the global acoustic feedback loop instantly modulates the shear layer upon separation for all the Mach number cases.

As the free-stream accelerates toward transonic regime (Mach 0.7 and 0.8), the acoustic energy intensifies and the spectral peaks become sharper, ultimately exceeding 155 dB at the trailing edge ($x/H = 6.25$) for the Mach 0.8 case for this cavity configuration. On top of that the entire baseline curve shifts upward - denotes the increase in broadband noise. Furthermore, lower-order modes (primarily Mode I) that remain indistinct at Mach 0.4 emerge prominently at transonic speeds. This demonstrates that an increase in compressibility not only amplifies the broadband noise, but also actively enforces stronger structural organization within the acoustic feedback loop.

A consistent trend observed at all streamwise locations is a shift of the dominant spectral peaks toward higher absolute frequencies with increasing Mach number; when expressed in terms of the convective

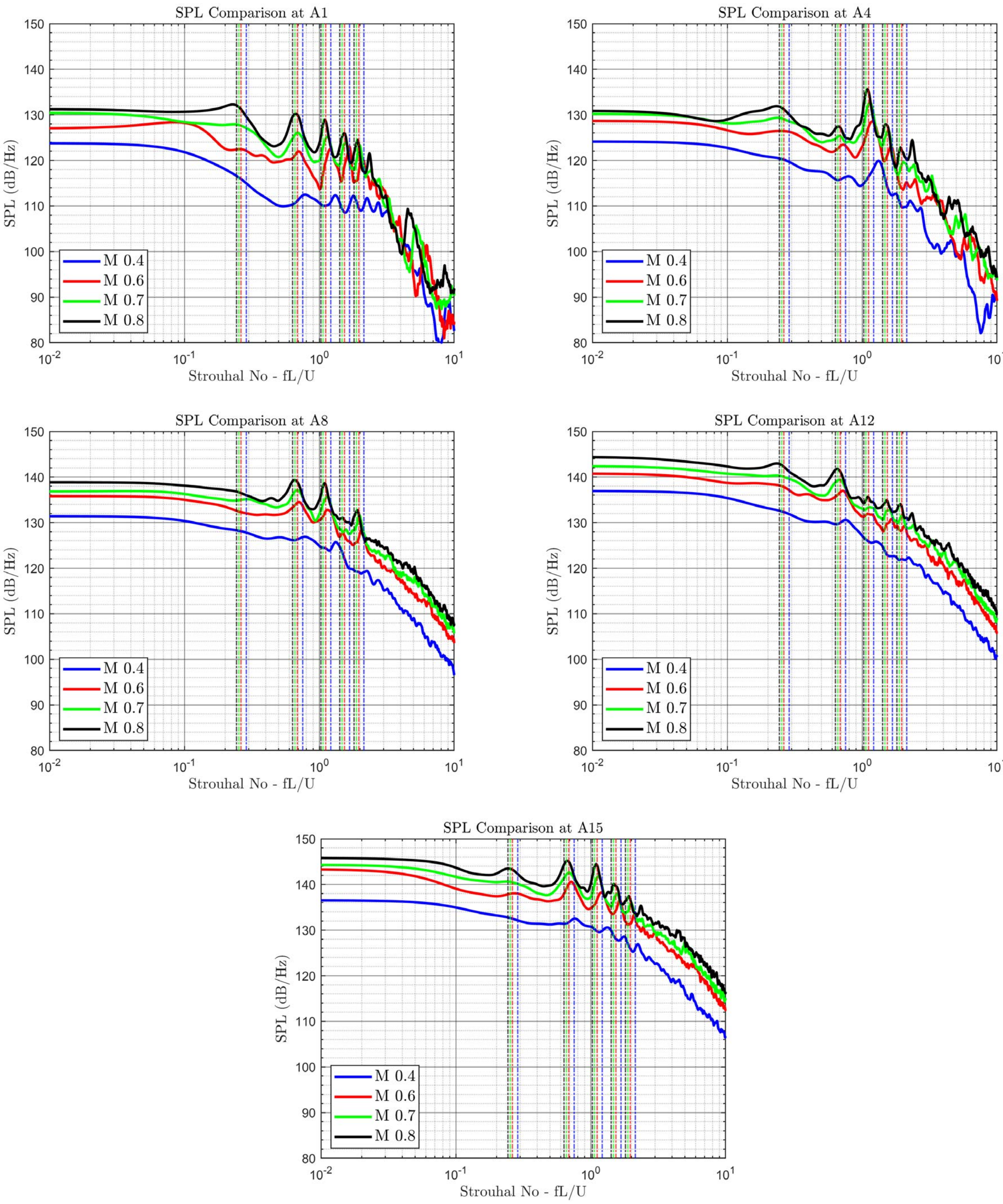


Figure 5: Comparison of SPL profiles at five locations on cavity top-Midplane

Strouhal number St=fL/U, this results in a systematic shift of the peaks toward lower values. This behaviour follows the empirical formula proposed by Rossiter [1]. Increasing Mach number lengthens the acoustic part of the feedback loop relative to convective scaling, which lowers the Strouhal number.

To evaluate the influence of compressibility on the time-averaged flow topology, the mean shear-layer development is shown in Fig. 6. At all nine streamwise locations ($x/H = 0.10 - 6.00$), the normalized mean velocity profiles ($U/U_{in}$) collapse closely onto one another over the entire Mach number range investigated ($M_\infty = 0.4 - 0.8$). The near-perfect overlap of the profiles indicates that the mean flow field exhibits negligible sensitivity to Mach number within the present operating range. Consequently, the overall shear-layer topology and its downstream evolution remain largely unchanged in a mean sense as the Mach number increases.

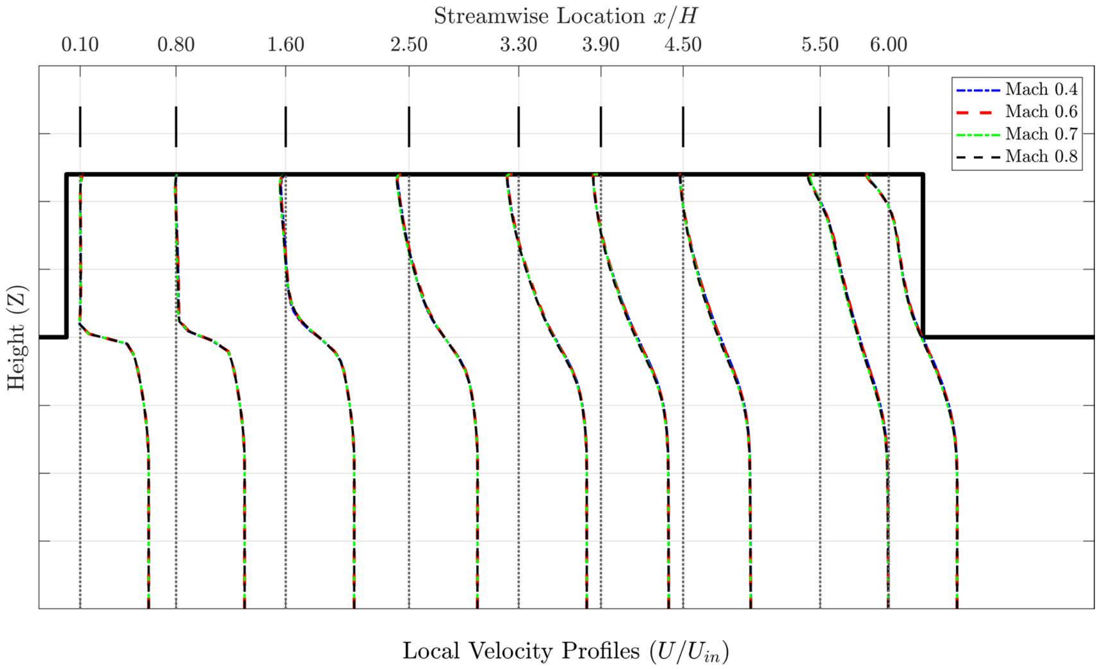


Figure 6: Mean non-dimensional velocity profiles at nine inside stations for all Mach numbers (50 percent)

This behavior is consistent with observations from compressible mixing-layer studies. For the present cavity configuration, the convective Mach number varies approximately between $M_c \approx 0.2$ and $0.4$ ($M_c \approx 0.5M_\infty$). According to the study of Papamoschou–Roshko [7], compressibility-induced suppression of shear-layer growth remains relatively weak in this regime, the dominant instability mechanisms continue to be governed by large-scale, two-dimensional Kelvin–Helmholtz spanwise vortices, resulting in only minor modifications to the mean shear-layer structure [8]. Therefore, accelerating the flow within this subsonic window does not fundamentally alter the time-averaged shear-layer topology. Instead, the primary effect of the increased Mach number is localized to the aeroacoustic domain, where the elevated kinetic energy acts strictly as a driver for intense acoustic resonance feedback loops within the cavity system.

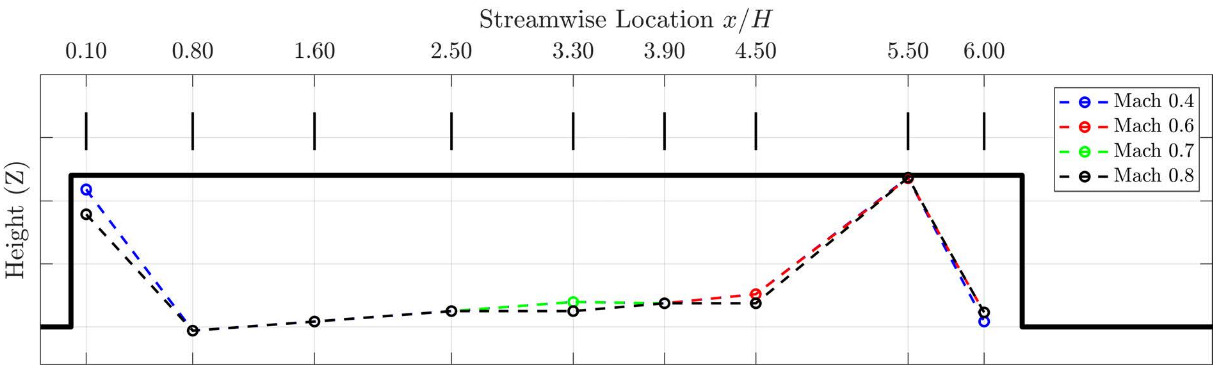


Figure 7: Location of Maximum $U_{\text{rms}}$ at all four Mach numbers for the nine locations

The spatial development of the unsteady flow field is illustrated in Fig. 7, which plots the wall-normal position ($y$) of the maximum streamwise velocity fluctuations ($U_{\text{rms}}$). Across all investigated Mach numbers, this peak unsteadiness follows the exact same spatial path along the cavity shear layer before shifting near the trailing edge. This perfect agreement indicates that the location of maximum unsteadiness is strictly determined by the mean flow geometry, independent of the Mach number. However, while their path is fixed, their amplitudes depend heavily on the Mach number. In Fig. 8(b), the OASPL curves rise in a nearly parallel fashion with increasing Mach number, showing that velocity primarily acts as a global scaling factor for the acoustic pressure field [6]. Conversely, the $U_{\text{rms}}$ amplitudes in Fig. 8(a) diverge as they move downstream. Though there is a convective growth for most part of the cavity length, they reduce sharply near the trailing edge for all the Mach cases. The sudden changes in the vertical location of the max $U_{\text{rms}}$ and their values as well as the alteration in the OASPL slope indicates the transition from simple convective growth to a direct hydrodynamic interaction with the aft wall.

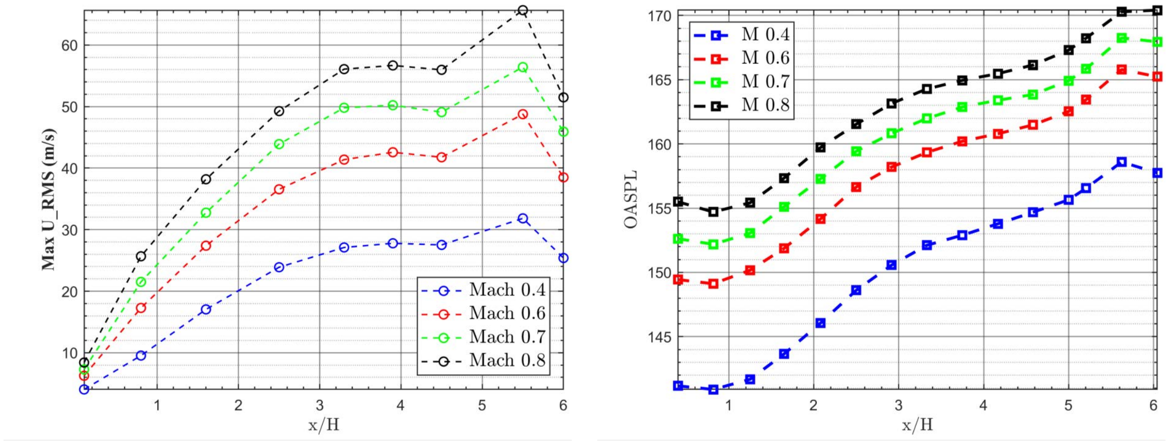


(a) (b)

Figure 8: Maximum $U_{\text{rms}}$ and OASPL throughout the cavity length at the mid-plane for all Mach numbers

However, because these spatial distributions are averaged over time, they blend all instantaneous variations together. The non – parallel distribution of max $U_{\text{rms}}$ curves suggests a possible average effect of mix of several Rossiter modes that varies with Mach number. Also, standard Fourier-based SPL spectra successfully identify the dominant Rossiter frequencies but they inherently assume that the underlying acoustic signal is stationary. Therefore, the simultaneous coexistence of multiple modes cannot be realized from those plots. To resolve this and understand the dynamic interaction of localized velocity fluctuation and acoustic pressure fluctuation, a non-stationary analysis is required.

### 3.2 Non-stationarity analysis

#### 3.2.1 Wavelet Spectral Power and its mean

The first step towards non – stationarity analysis is to plot instantaneous Normalized Wavelet Spectral Power (WSP). For that, a Continuous Wavelet Transform (CWT) is applied to the high-frequency pressure data. The mean-detrended pressure fluctuation, ($p'(t) = p(t) - \bar{p}$) is convoluted with an analytic Morlet wavelet. The wavelet transform is defined as

$$W(s,\tau) = \frac{1}{\sqrt{s}} \int_{-\infty}^{\infty} p'(t)\, \psi^*\left(\frac{t-\tau}{s}\right)\, dt,$$

where $s$ is the wavelet scale, $\tau$ is the translation parameter, $\psi$ is the mother wavelet, and $(\cdot)^*$ denotes the complex conjugate. To interpret the acoustic dynamics physically, the scale-translation domain is mapped to the time-frequency domain. Mapping the coefficients to the time-frequency domain yields $W(f,t)$. The instantaneous Wavelet Spectral Power (WSP) is then formally computed as the squared magnitude of the complex coefficients:

$$P_w(f,t) = |W(f,t)|^2$$

To illustrate the fundamental differences in flow organization, the time-frequency contours are presented for two representative locations: A1 (near the leading edge) and A8 (mid-cavity) for three Mach numbers,

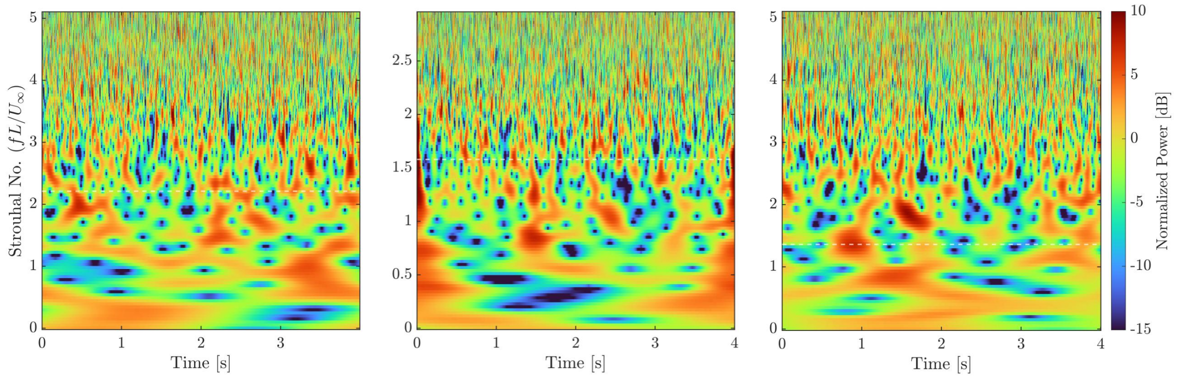


(a)

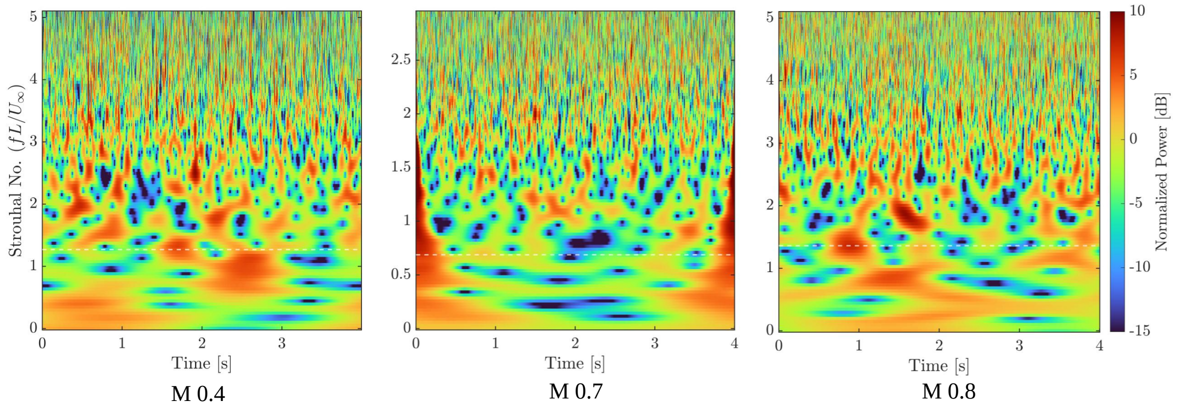


(b)

Figure 9: Normalized Wavelet Spectral power for (a) A1 and (b) A8

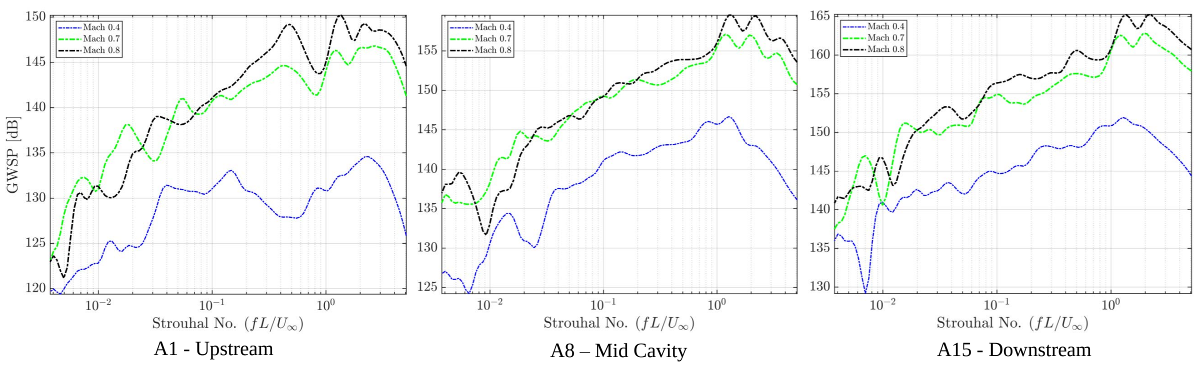


Figure 10: Global WSP for three locations

0.4, 0.7 and 0.8 (Fig.9). The acoustic energy appears as discrete, short-lived bursts. This visually highlights the highly intermittent nature of the acoustic feedback loop, indicating that the energy is dominated by transient events rather than a steady emission.

To quantify the time-averaged energy of the transient flow features, the Global Wavelet Spectral Power (GWSP) was computed by time-averaging the linear wavelet power across the entire signal and converting it to standard acoustic decibels (Fig.10). Both the standard SPL and the GWSP provide time-averaged measures of spectral energy and capture the primary Rossiter peaks. However, the GWSP is obtained from a temporally localized wavelet representation and therefore serves as a natural bridge between conventional spectral analysis and the subsequent time-frequency characterization of the cavity dynamics. While the

GWSP provides a spectral description comparable to the SPL, the underlying wavelet representation additionally retains the temporal evolution of the energetic events, which is subsequently exploited to quantify modal intermittency, persistence, and structural organization.

### 3.2.2 Spectral Entropy

To quantify the degree of organization within the acoustic field, the time-resolved Shannon Spectral Entropy was computed from the instantaneous Wavelet Spectral Power. At each time step, the linear wavelet power, $P_w(f,t)$, is normalized to yield a spectral probability density function, $p(f,t)$:

$$p(f,t) = \frac{P_w(f,t)}{\sum_f P_w(f,t)}$$

The time-resolved entropy, $H(t)$, is then calculated to evaluate the instantaneous distribution of spectral energy. To bound the metric between 0 and 1, it is normalized by the theoretical maximum entropy corresponding to the total number of frequency bins ($N_f$):

$$\hat{H}(t) = \frac{-\sum_f p(f,t)\ln p(f,t)}{\ln(N_f)}$$

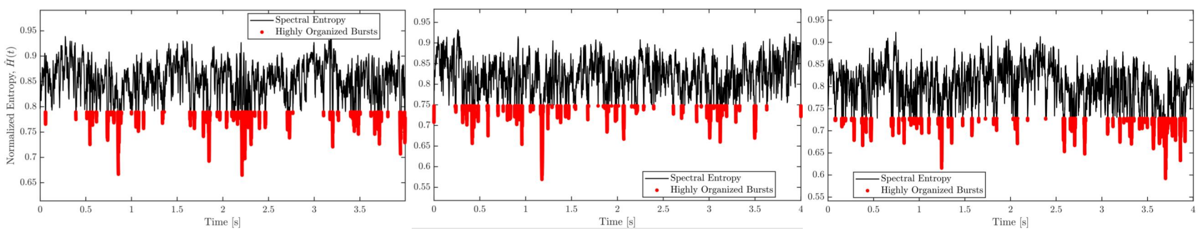


M 0.4 M 0.7 M 0.8

Figure 11: Time resolved spectral entropy at A15 - near trailing edge

A normalized entropy value approaching 1 indicates highly disorganized, broadband turbulence, whereas sudden drops in entropy mark the onset of highly organized, tonal acoustic resonance. As illustrated in Fig.11, for the trailing edge location at three Mach numbers, the flow does not maintain a steady state; instead, the shear layer exhibits intense, intermittent entropy drops, confirming a continuous switching between disorganized turbulence and highly organized acoustic bursting. To visually isolate these events, entropy values falling below an approximate threshold of $\mu - 1.5\sigma$ are highlighted as highly organized bursts.

Crucially, a visual inspection of the entropy time-series reveals that the entire signal appears to ride on a continuous, slow undulation that is clearly visible to the naked eye. To rigorously quantify this visually apparent slow modulation, a low-pass Butterworth filter (cutoff frequency of 10 Hz) was applied to the detrended entropy signal. Welch's Power Spectral Density (PSD) of this filtered envelope (Fig.12) reveals a discrete set of multiple low-frequency peaks (e.g., below 10 Hz) across all Mach numbers.

Mathematically, a stochastic process is stationary if its statistical properties are invariant under a shift in time. In such a case, the spectral probability density, $p(f,t)$, remains statistically unchanged and the normalized entropy fluctuates only randomly about a constant mean value, i.e.,

$$[\hat{H}(t) = C + \epsilon(t),]$$

where $C$ is a constant and $\epsilon(t)$ represents bounded random fluctuations with no coherent temporal modulation. In contrast, the presence of persistent low-frequency oscillations in $\hat{H}(t)$ implies that the

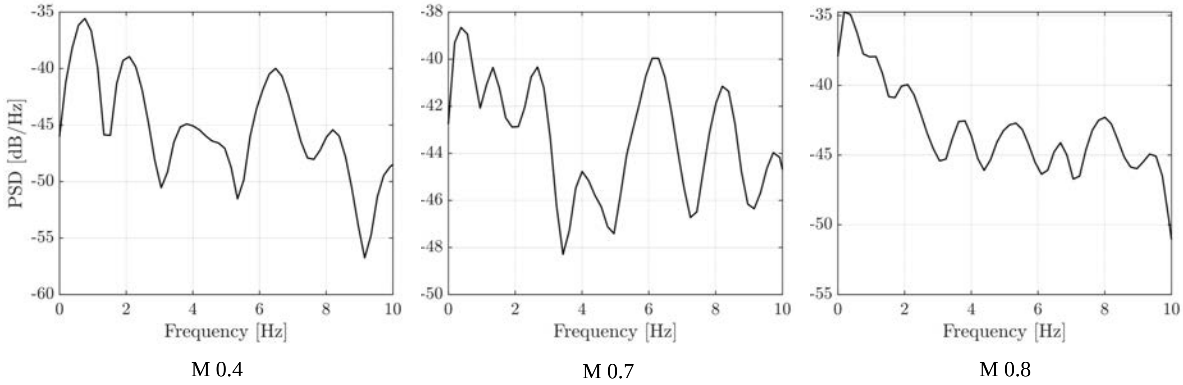


Figure 12: Low frequency modulation of the entropy

spectral organization continuously evolves on time scales much longer than the Rossiter periods. The normalized spectral entropy therefore deviates from a stationary constant and instead exhibits a slowly varying breathing envelope, demonstrating that the compressible cavity dynamics are intrinsically non-stationary [9]. To the authors' knowledge, explicitly quantifying this low-frequency breathing envelope through spectral entropy analysis has not been previously reported for compressible cavity flows.

### 3.2.3 Ridge extraction and clustering

To track the dominant coherent structures in real-time, continuous wavelet ridge extraction was employed. A wavelet transform unfolds the 1D pressure signal into a 2D time-frequency plane, yielding the continuous wavelet spectral power $P_w(f,t)$.

At any given time $t$, the dominant aeroacoustic mechanism is correspond to the frequency scale that exhibits maximum localized energy. The instantaneous dominant frequency, $f_{ridge}(t)$, is thus extracted by locating the global maximum across the frequency band of interest at each time step:

$$f_{ridge}(t) = \arg\max_{f} P_w(f,t)$$

All extracted ridges provide a continuous instantaneous Strouhal number, $St(t) = f_{ridge}(t)L/U_\infty$. This contain the frequencies correspond to high energy acoustic noise and broadband noise because the algorithm blindly tracks the highest-amplitude stochastic noise spike. This may falsely inflate the lifespan of tonal modes [10, 11].

Similar to the variance based bursting detection technique by Blackwelder and Kaplan [12], which detects bursting events by thresholding a localized variance signal, the present approach identifies Rossiter lock-ins from the broadband noise by utilizing a threshold for the instantaneous wavelet ridge power. In both cases, coherent intermittent events are extracted from a stochastic background using an energy-based discriminator. A mode is considered physically active only if its instantaneous ridge power, $P_{max}(t)$, exceeds a threshold defined by:

$$\tau = \mu_P + 0.5\sigma_P$$

where $\mu_P$ and $\sigma_P$ are the mean and standard deviation of the ridge power time-series, respectively. A sensitivity analysis of the present dataset (a profile is shown in Fig.13 for A8 at Mach 0.8 for better understanding) indicates that a coefficient of 0.5 provides a reasonable compromise between retaining coherent bursts and suppressing low-energy fluctuations.

To analyze the statistical data and ultimately to evaluate Markov survival probabilities of the cavity, the

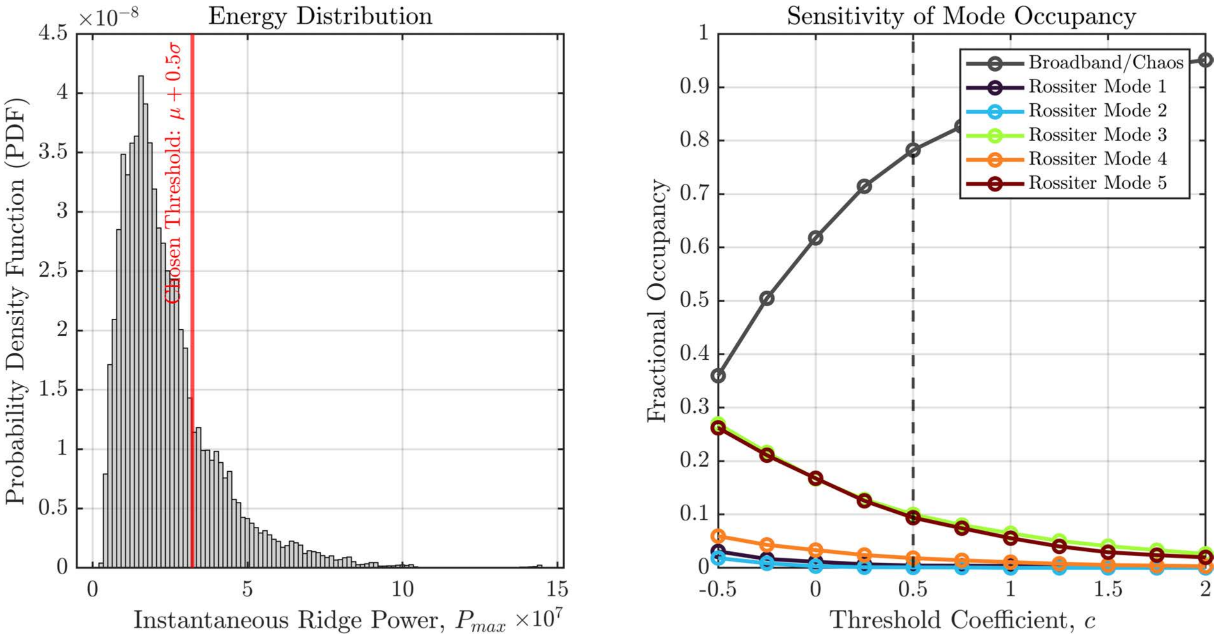


Figure 13: Threshold sensitivity for clustering - at A8 M 0.8

continuous instantaneous Strouhal signal must be discretized into finite physical states. In data-driven fluid dynamics, unsupervised machine learning algorithms (such as K-Means clustering) are frequently utilized to partition continuous time-series data into discrete kinematic clusters [13].

However, unsupervised clustering methods are driven by data density rather than physical constraints. In intermittent cavity flows, some Rossiter modes may be weakly populated or entirely absent, causing K-means to generate non-physical clusters by splitting existing modes to artificial tonal states. Therefore, a supervised distance-based classifier anchored to the theoretical Rossiter frequencies was employed.

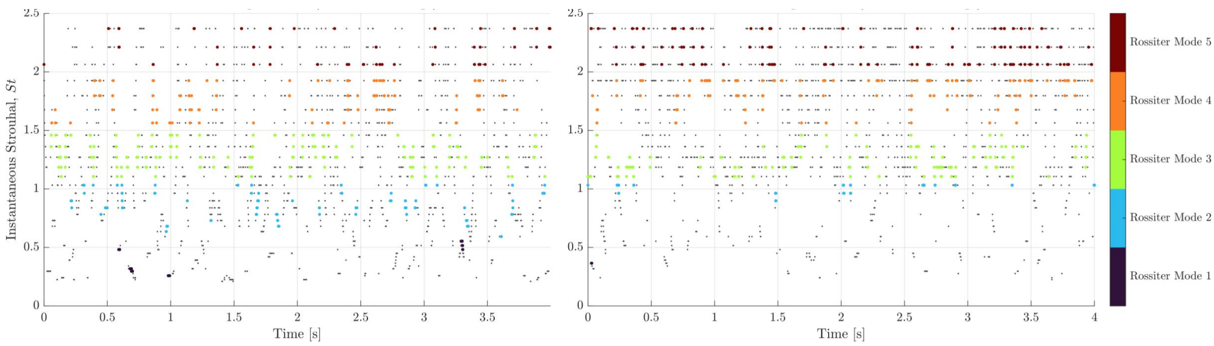


M 0.4 M 0.7

Figure 14: Clustering of modes - at A15

Using a minimum Euclidean distance criterion, each time step $t$ was mathematically classified into either a discrete Rossiter mode ($n = 1, 2, 3...$) or, if the energy threshold was not met, the broadband spectrum. The same has been plotted in Fig.14 for A15 location for two Mach numbers. This procedure ensures that the clustering does not fall prey to the algorithmic artifacts.

### 3.2.4 Survival Probability of the Modes

To mathematically characterize the temporal stability of the aeroacoustic feedback loop, an empirical survival probability analysis, $P(T > t)$, was conducted for each active state and compared against a theoretical First-Order Markov process. In a purely memoryless system, survival follows an exponential decay model:

$$S(t) = \exp(-t/\tau_k)$$

where, $\tau_k$ is the theoretical Markov time constant.

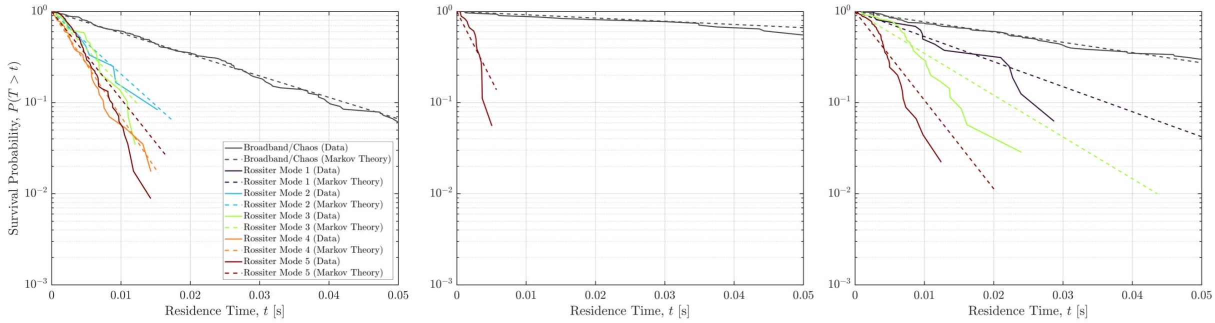


(a)

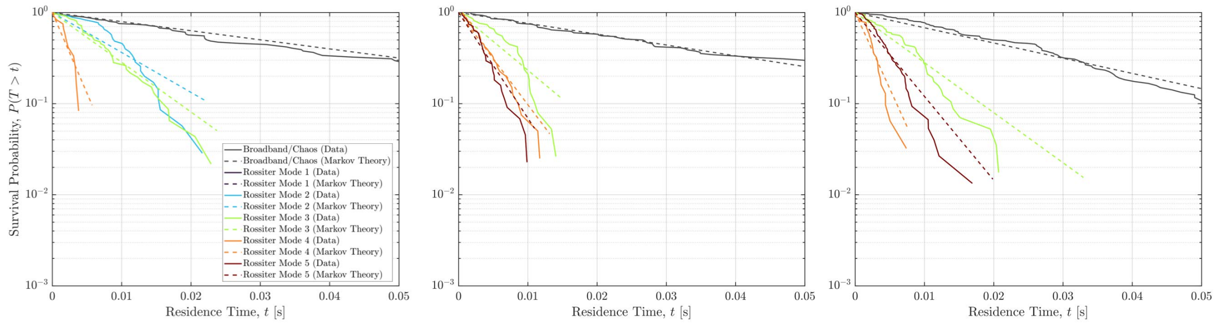


(b)

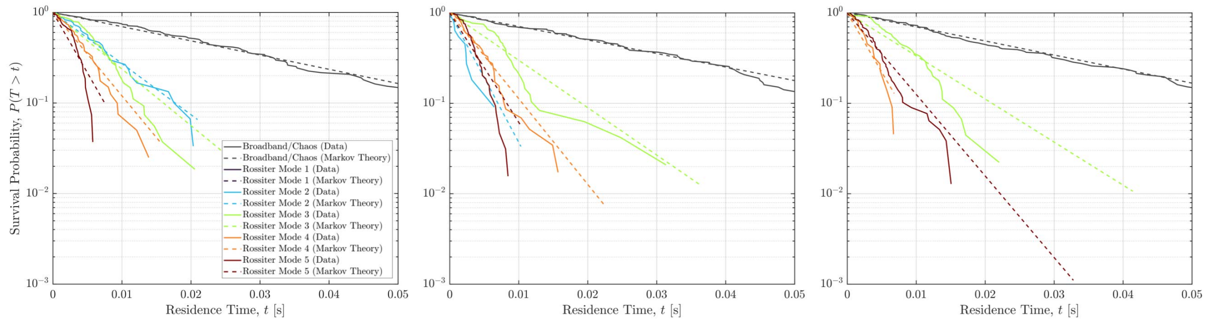


M 0.4 M 0.7 M 0.8

(c)

Figure 15: Survival probability of acoustic modes at (a) A1 (b) A8 and (c) A15

The approximately exponential decay during the intermediate residence time indicates that a first-order Markov model provides a reasonable statistical description of modal switching. Nevertheless, a systematic departure from ideal memoryless behavior is evident. At larger residence times, the empirical survival probability falls below the exponential Markov prediction, indicating that highly persistent modal states are less probable than expected from a purely memoryless process. This accelerated decay suggests the presence of additional deterministic mechanisms that limit the maximum persistence of coherent lock-in states. In particular, low-frequency modulations of the cavity flow that we discussed earlier may alter the shear-layer trajectory and periodically disrupt the hydrodynamic–acoustic feedback loop, thereby preventing tonal modes from remaining locked-in for arbitrarily long durations. Finally, it indicates that cavity modal dynamics are not strictly memoryless but are more appropriately described as finite-memory, quasi-Markovian processes.

Across all operating conditions, the broadband state exhibits the largest residence times and remains the statistically dominant configuration, whereas the Rossiter modes are comparatively transient and exhibit significantly shorter residence times. This residence-time hierarchy is consistent with the wavelet spectrum (Fig.9), in which broadband activity forms a nearly continuous background while organized Rossiter ridges appear intermittently as localized episodes of modal lock-in.

Although the SPL spectra (Fig.5) exhibit distinct Rossiter peaks, they do not indicate how long these modes persist in time. The wavelet spectra qualitatively show that the Rossiter modes occur intermittently, whereas the survival analysis quantifies their residence times and reveals pronounced streamwise variations in modal persistence. Individual Rossiter modes appear, disappear, and reappear at different sensor locations, indicating that the cavity dynamics are highly non-uniform along the cavity length.

Increasing Mach number does not produce a universal monotonic reduction in modal persistence. Instead, increasing compressibility redistributes the relative stability of competing Rossiter states, with the persistence of individual modes depending strongly on both Mach number and streamwise location. Lower-order modes frequently become more intermittent at several high-Mach operating conditions, whereas higher-order modes, particularly Rossiter Mode 5, can exhibit increased occupancy and persistence.

However, Throughout all conditions, the broadband state remains the dominant long-lived configuration, indicating that increasing compressibility reorganizes rather than completely suppresses the cavity's modal dynamics.

#### 3.2.5 Conditional Statistics of Acoustic Power and Structural Coherence

Finally, conditional statistics were extracted to examine whether coherent tonal events differ primarily in their average power level or in their spectral organization. For any continuous lock-in event r of mode k spanning a residence time $\Delta t_r = t_{\text{end}} - t_{\text{start}}$, the mean tonal power, $(\Pi_r)$, was computed by averaging the instantaneous wavelet ridge power, $P_{\max}(t)$, over the duration of the event:

$$\Pi_r = \frac{1}{\Delta t_r} \int_{t_{\text{start}}}^{t_{\text{end}}} P_{max}(t)dt \tag{1}$$

Simultaneously, the instantaneous spectral distribution was quantified using normalized Shannon entropy to evaluate the structural coherence of the shear layer. The normalized spectral entropy, $\hat{H}(t)$, defined in Section 3.2.2, was further averaged over each continuous lock-in event to quantify its mean structural coherence. For a burst of duration $\Delta t_r = t_{\text{end}} - t_{\text{start}}$, the event-averaged entropy is defined as

$$\hat{H}_r = \frac{1}{\Delta t_r} \int_{t_{\text{start}}}^{t_{\text{end}}} \hat{H}(t)\, dt. \tag{2}$$

Thus, while $\hat{H}(t)$ characterizes the instantaneous spectral organization of the acoustic field, $\hat{H}_r$ represents the average degree of organization maintained throughout an entire lock-in episode.

where $\hat{H} \to 1$ denotes a completely disorganized, broadband energy distribution, and $\hat{H} \to 0$ denotes a perfectly coherent, singular tonal peak. To evaluate the temporal evolution of these metrics, the extracted events were conditionally partitioned into "Short Lifespan" and "Long Lifespan" populations, bifurcated by the median residence time for each respective mode. To strictly isolate the coherent aeroacoustic resonance, the broadband noise state was explicitly excluded from this distribution.

Spatially, the absolute magnitude of the acoustic saturation $(\Pi_r)$ steadily increases from the leading edge

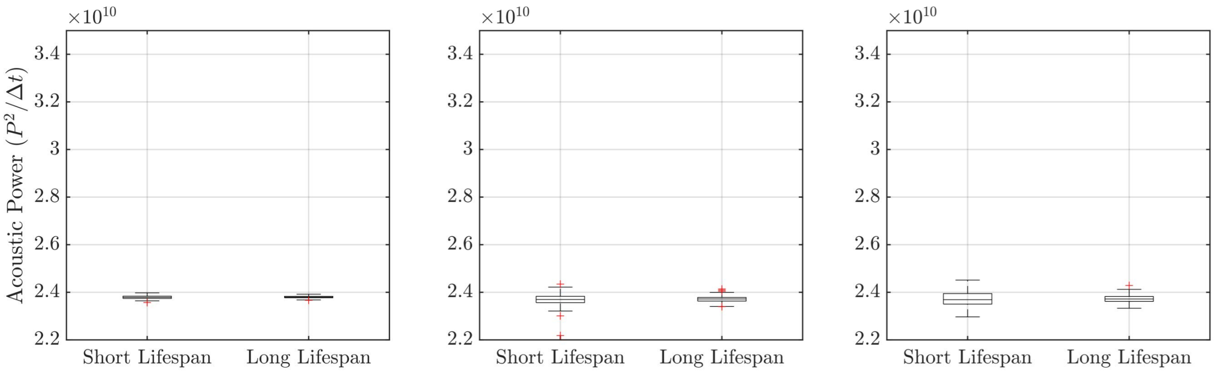


(a)

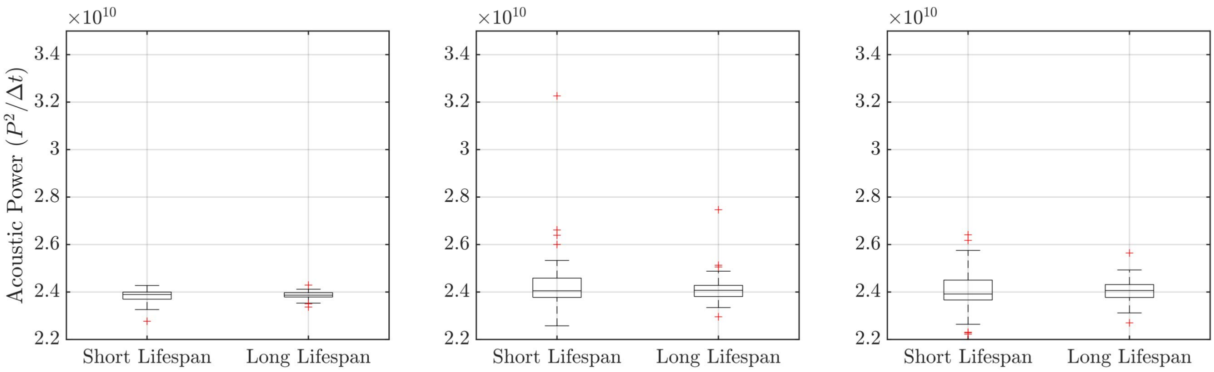


(b)

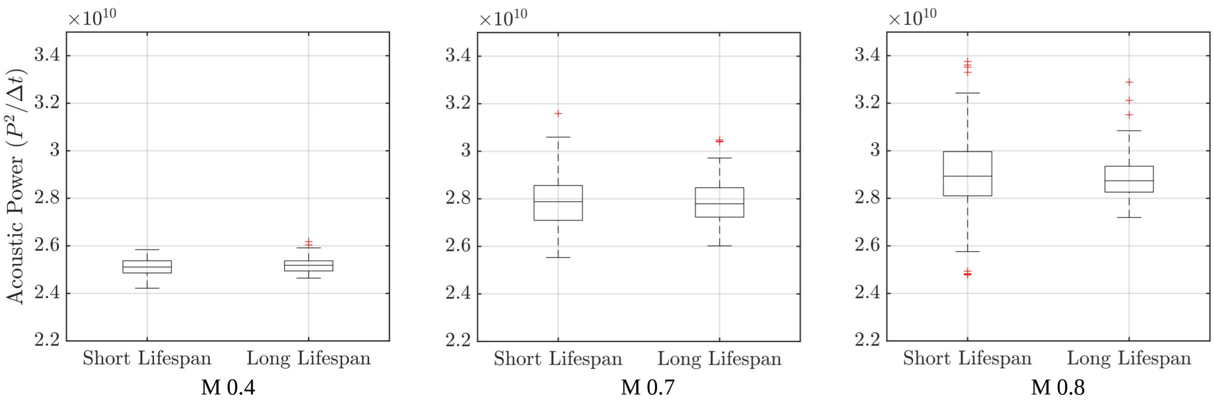


(c)

Figure 16: Box plots of mean tonal power for short- and long-lived lock-in events at (a) A1 (b) A8 and (c) A15 (broadband states are excluded)

(A1) toward the trailing edge (A8 and A15), independent of freestream Mach number (Fig.16). This spatial amplification quantitatively models the convective growth of the Kelvin-Helmholtz instability. It mathematically confirms that the violent mass-flux impingement at the aft wall serves as the primary acoustic generation mechanism.

The median acoustic power (Fig.16) remains nearly unchanged between short- and long-lived tonal events. This weak dependence on burst duration suggests that the cavity behaves similarly to a nonlinear self-sustained oscillator: once a Rossiter mode is established, its amplitude grows rapidly and then approaches a characteristic saturated level. The mode subsequently persists near this level until the feedback loop is disrupted. In other words, a longer-lived tonal event does not continue to gain energy indefinitely; rather,

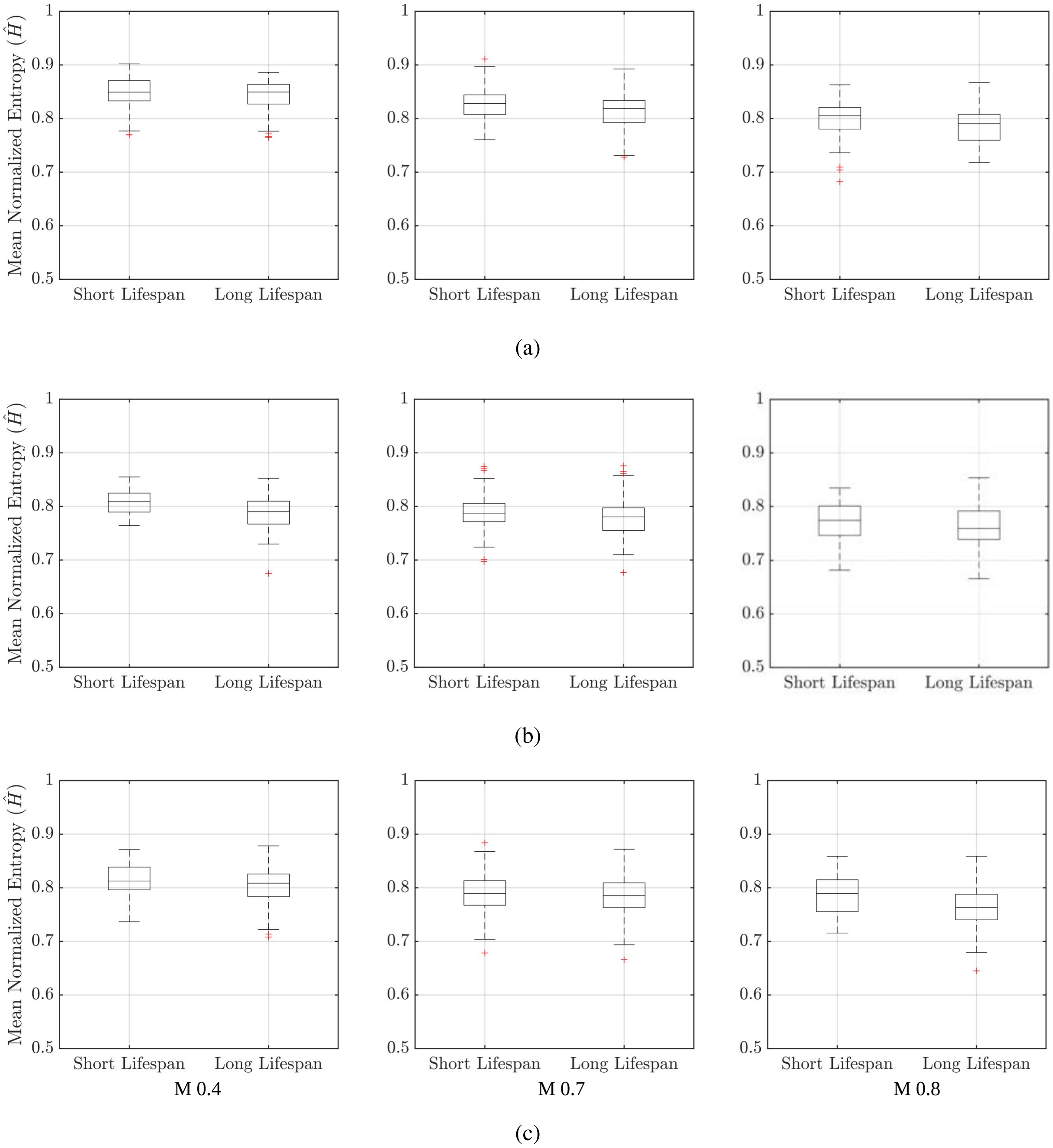


Figure 17: Box plots of structural coherence for short- and long-lived lock-in events at (a) A1 (b) A8 and (c) A15 (broadband states are excluded)

it simply remains phase-locked for a longer time before the feedback interaction breaks down and the mode disappears.

Considering only coherent tonal episodes (with the broadband state excluded), increasing the Mach number systematically increases the median mean tonal power of the surviving Rossiter lock-in events. The increase is modest near the leading edge (A1) but becomes progressively larger downstream, reaching approximately 10% at A8 and A12 and nearly 15–20% at A15 as $M_\infty$ increases from 0.4 to 0.8. At the same time, the median normalized entropy exhibits a systematic reduction, decreasing by approximately 8–10% at A1 and by approximately 5–10% at downstream locations (Fig.17). Moreover, for a given Mach number, the mean tonal power differs only weakly between short- and long-lived events, whereas the entropy consistently shifts toward lower values for the long-lived episodes, indicating slightly greater spectral organization for long lived events than short-lived ones.

To quantify how much time the system spends in each state, the occupancy was computed as the percentage of the total record assigned to that state, including the broadband state.

Table 1: Occupancy (%) of the broadband state and Rossiter modes at selected sensor locations.

| Location | $M_\infty$ | Broadband | R1 | R2 | R3 | R4 | R5 |
|---|---|---|---|---|---|---|---|
| A1 | 0.4 | 75.66 | 0.38 | 1.90 | 3.85 | 5.37 | 12.84 |
| A1 | 0.7 | 94.96 | 1.19 | 0.15 | 1.69 | 0.77 | 1.23 |
| A1 | 0.8 | 80.09 | 6.32 | 0.05 | 8.05 | 0.47 | 5.02 |
| A8 | 0.4 | 79.50 | 1.42 | 8.68 | 9.16 | 0.74 | 0.50 |
| A8 | 0.7 | 82.29 | 1.44 | 1.44 | 6.51 | 4.29 | 4.03 |
| A8 | 0.8 | 77.97 | 0.00 | 0.11 | 11.06 | 2.01 | 8.85 |
| A15 | 0.4 | 76.84 | 1.15 | 5.78 | 9.39 | 4.72 | 2.12 |
| A15 | 0.7 | 76.84 | 0.08 | 0.76 | 9.94 | 6.64 | 5.75 |
| A15 | 0.8 | 78.24 | 0.43 | 0.09 | 10.03 | 1.82 | 9.39 |

As summarized in Table 1, the broadband state remains the dominant part, accounting for approximately 75–80% of the total record at most sensor locations and Mach numbers, with the notable exception of the leading-edge location at $M_\infty = 0.7$, where its occupancy approaches 95%.

Furthermore, no systematic monotonic trend is observed in occupancy with increasing Mach number. Instead, increasing compressibility redistributes the relative occupancy among competing Rossiter modes in a location-dependent manner, while keeping the overall dominance of the broadband state almost constant.

## 4. Conclusion

From the discussions till now, it is well understood that despite the substantial increase in SPL with the Mach number, the occupancy of the broadband and coherent states remains comparatively unchanged at most sensor locations. This indicates that the cavity does not become louder simply because it spends more time in tonal lock-in states. Instead, the conditional statistics show that the surviving Rossiter episodes become progressively more energetic, while the accompanying reduction in entropy indicates that these episodes are increasingly spectrally organized. Thus, the rise in SPL is primarily associated with energetic amplification and structural reorganization of the coherent states rather than a fundamental increase in their temporal occupancy.

This statistical picture also helps explain why active control becomes increasingly difficult at higher Mach numbers [14, 15]. Although higher Mach numbers demand more powerful and faster actuators because of the increased flow energy and pressure, the more fundamental challenge arises from the temporal organization of the cavity dynamics. The conditional statistics indicate that the surviving locked-in modes become somewhat more energetic and slightly more spectrally organized, which, in principle, could make them easier to identify and target. However, the survival and occupancy statistics show that these coherent episodes remain intermittent and embedded within a largely dominant broadband background even at Mach 0.8, while the modal switching behaviour remains approximately quasi-Markovian over intermediate time scales. Consequently, a controller must continuously identify and react to stochastic transitions between competing states rather than suppress a single persistent resonance, and the modest increase in coherence is insufficient to compensate for the simultaneously increasing energetic requirements of actuation.

As an alternative solution, passive approaches that modify the incoming boundary layer [6] act directly on the resonance mechanism itself and therefore offer a more robust means of mitigating cavity oscillations under high-Mach conditions.

## 5. Acknowledgements

Authors would like to acknowledge the partial support from Aeronautical Development Establishment, Bangalore to carry out this work through the SID project PC 99590. They also like to thank SERC, IISc Bangalore in constantly supporting by providing computational facility.

## References

[1] J. E. Rossiter. Wind tunnel experiments on the flow over rectangular cavities at subsonic and transonic speeds. Technical report, Aeronautical Research Council, Reports and Memoranda, AERADE, 1964. Accessed: 2026-01-XX.

[2] Y. Sun, K. Taira, L. N. Cattafesta III, and L. S. Ukeiley. Biglobal instabilities of compressible open-cavity flows. *Journal of Fluid Mechanics*, 826:270–301, 2017.

[3] Marlon Sproesser Mathias and Marcello A. F. Medeiros. The effect of incoming boundary layer thickness and mach number on linear and nonlinear rossiter modes in open cavity flows. *Theoretical and Computational Fluid Dynamics*, 35:495–513, 2021.

[4] S&I Engineering Solutions Pvt. Ltd. HiFUN: A Parallel CFD Flow Solver. https://sandi.co.in/, 2026. Accessed: February 17, 2026.

[5] Tomer Rokita, Yossef Elimelech, Rimon Arieli, Yuval Levy, and J. B. Greenberg. Experimental characterization of turbulent subsonic transitional–open cavity flow. *Experiments in Fluids*, 57, 2016.

[6] Argha Saha, O. N. Ramesh, and N. Balakrishnan. Effect of upstream boundary layer thickness on cavity acoustics. In *32nd AIAA/CEAS Aeroacoustics Conference*, 2026.

[7] Dimitri Papamoschou and Anatol Roshko. The compressible turbulent shear layer: An experimental study. *Journal of Fluid Mechanics*, 197:453–477, 1988.

[8] R. Sauvage and A. Kourta. Compressible effects on a temporal direct numerical simulation. In *ESAIM: Proceedings, Third International Workshop on Vortex Flows and Related Numerical Methods*, volume 7, pages 378–386, 1999.

[9] Osvaldo A. Rosso, Susana Blanco, Juliana Yordanova, Vilislav Kolev, Alejandra Figliola, Michael Schürmann, and Erol Başar. Wavelet entropy: A new tool for analysis of short duration brain electrical signals. *Journal of Neuroscience Methods*, 105(1):65–75, 2001.

[10] René Carmona, Wen-Liang Hwang, and Bruno Torrésani. Characterization of signals by the ridges of their wavelet transforms. *IEEE Transactions on Signal Processing*, 45(10):2586–2590, 1997.

[11] Hasan Kamliya Jawahar, Stefano Meloni, Roberto Camussi, and Mahdi Azarpeyvand. Intermittent and stochastic characteristics of slat tones. *Physics of Fluids*, 33(2):025120, 2021.

[12] R. F. Blackwelder and R. E. Kaplan. On the wall structure of the turbulent boundary layer. *Journal of Fluid Mechanics*, 76(1):89–112, 1976.

[13] Eurika Kaiser, Bernd R. Noack, Laurent Cordier, Andreas Spohn, Marc Segond, Markus Abel, Guillaume Daviller, Janos Östh, Sinisa Krajnović, and Robert K. Niven. Cluster-based reduced-order modelling of a mixing layer. *Journal of Fluid Mechanics*, 754:365–414, 2014.

[14] Louis N. Cattafesta III, Qi Song, David R. Williams, Clarence W. Rowley, and Farrukh S. Alvi. Active control of flow-induced cavity oscillations. *Progress in Aerospace Sciences*, 44(7–8):479–502, 2008.

[15] Clarence W. Rowley and David R. Williams. Dynamics and control of high-reynolds-number flow over open cavities. *Annual Review of Fluid Mechanics*, 38:251–276, 2006.